Correlation between deep-level defects and functional properties of β-(Sn$_x$Ga$_{1-x}$)$_2$O$_3$ on Si photodetectors

Isa Hatipoglu,[1] [iD] Daniel A. Hunter,[2] [iD] Partha Mukhopadhyay,[1] [iD] Martin S. Williams,[2] [iD] Paul R. Edwards,[2] [iD] Robert W. Martin,[2] [iD] Winston V. Schoenfeld,[1,3,4,a)] [iD] and G. Naresh-Kumar[2,b)] [iD]

AFFILIATIONS

[1]CREOL, The College of Optics and Photonics, University of Central Florida, Orlando, Florida 32816, USA
[2]Department of Physics, SUPA, University of Strathclyde, Glasgow G4 0NG, United Kingdom
[3]Department of Electrical and Computer Engineering, University of Central Florida, Orlando, Florida 32816, USA
[4]Department of Materials Science and Engineering, University of Central Florida, Orlando, Florida 32816, USA

Note: This paper is part of the Special Topic on Wide Bandgap Semiconductor Materials and Devices.
[a)]winston@ucf.edu
[b)]**Author to whom correspondence should be addressed:** naresh.gunasekar@strath.ac.uk

ABSTRACT

Heterogeneous integration of β-(Sn$_x$Ga$_{1-x}$)$_2$O$_3$ (TGO) UV-C photodetectors on silicon substrates by molecular beam epitaxy is demonstrated. Multimodal electron microscopy and spectroscopy techniques reveal a direct correlation between structural, compositional, and optical properties of TGO and the functional properties of the photodetectors. Wavelength dispersive x-ray spectroscopy results accurately determine Sn concentrations (x) in the region of 0.020, and room temperature cathodoluminescence (CL) hyperspectral imaging shows changes in the CL emission intensity in TGO compared with a Ga$_2$O$_3$ sample with no Sn. Alloying Ga$_2$O$_3$ with Sn is shown to quench the red emission and enhance the blue emission. The increase in blue emission corresponds to the rise in V$_{Ga}$-related deep acceptors responsible for the high gain observed in the TGO detectors. A Ga$_2$O$_3$ nucleation layer is shown to improve the TGO surface quality and give better device properties compared to TGO grown directly onto the Si substrate, including a higher specific detectivity on the order of 10^{12} Jones.

I. INTRODUCTION

The UV spectrum covers a wide range of wavelengths spanning 10–400 nm. The earth's atmosphere and ozone absorb UV-C (100–280 nm), removing radiation with wavelengths shorter than 280 nm from the solar spectrum that reaches its surface. Therefore, a detector designed to be sensitive to only these wavelengths is not affected by solar radiation and is said to be solar-blind. Solar-blind photodetectors have numerous applications, including in missile guidance systems, flame detection,[1] underwater communication,[2] and astrophysics.[3] Several binary wide bandgap semiconductors, including AlN, BN, diamond, and ternary materials, such as Al$_x$Ga$_{1-x}$N, and Mg$_x$Zn$_{1-x}$O, have been used to develop solar-blind photodetectors.[4–6] Among these materials, Ga$_2$O$_3$ is a promising new contender set to dominate the semiconductor industry due to its ultra-wide bandgap of ≈4.8 eV[7] as well as the ability to tune the bandgap from ≈3 to 6 eV by alloying with In$_2$O$_3$[8,9] or Al$_2$O$_3$.[10] In addition to photodetectors, these materials have potential applications in high power and high frequency electronic devices[11] as well as in optical waveguides.[12] The laser-induced damage threshold of Ga$_2$O$_3$ is comparable with other high-threshold materials such as SiO$_2$ and Al$_2$O$_3$, making Ga$_2$O$_3$ waveguides a potential candidate for high-power integrated photonics.[13] While alloying Ga$_2$O$_3$ with indium (In) could tailor the bandgap and shift the detector responsivity to the UV-B region, the relative rarity of In compared to Sn makes the latter an attractive alternative. The abundance of Sn in the Earth's upper continental crust is 2.2 ppm, whereas it is

0.25 ppm for In.[14] Moreover, the adjacency of In and Sn in the periodic table results in In 3^+ and Sn 4^+ ions in Ga_2O_3 having the same electronic structure. Recent studies have shown that alloying Sn with β-Ga_2O_3 dramatically increases the peak responsivity and cut-off wavelengths of Ga_2O_3-based UV–C photodetectors.[15–17] The high peak responsivities are associated with high gains, which are generally attributed to impact ionization[18] and self-trapped holes (STH) via Schottky barrier lowering.[19] Impact ionization is a very unlikely mechanism with the low bias voltages due to the low peak electric field strength (typically $< \approx 2$ MeV/cm with hole mobility $< 10^{-10}$ cm^2 V^{-1} s^{-1})[20] compared to the 8 MeV/cm breakdown voltage of Ga_2O_3.[7] Furthermore, STH may not be a prominent effect at room temperature as STH were shown to be thermally unstable above 90 K.[21] It is possible that deep intra-band acceptor states, especially gallium vacancies (V_{Ga}) and their complexes may serve as trapping sites for holes.[22] Alloying can be used for introducing deep acceptors in the material system as well as increasing the UV–C coverage and improving the bandwidth of the resulting photodetector. Previously, $(Sn_xGa_{1-x})_2O_3$ (TGO) photodetectors were fabricated on sapphire[15] and bulk Ga_2O_3 substrates.[16] However, the use of silicon as a substrate offers several key advantages, such as cost and the enabling of monolithic integration with silicon electronics and photonics.[23] Here, we demonstrate for the first time the feasibility of producing TGO on Si substrates by molecular beam epitaxy (MBE) and correlate the devices' structural, optical, and functional properties using multimode electron microscopy and spectroscopy methods. We study the effects of a Ga_2O_3 buffer layer beneath the TGO thin film. We also study the role of the deep acceptor states introduced by Sn alloying and their role in the increased photodetector gain. This work presents new possibilities for producing large area TGO based UV detectors and Ga_2O_3-based heterojunction p–n structures on the Si platform and provides new insight into the gain mechanisms in such devices.

II. EXPERIMENTAL SECTION

TGO films are grown by plasma-assisted MBE on n-type (n $\approx 10^{18}$ cm^{-3}) (111) Si substrates. Results from three samples (1) Ga_2O_3 grown directly on the Si substrate (sample A), (2) TGO grown directly on the Si substrate (sample B), and (3) TGO grown on a Ga_2O_3 buffer layer on the Si substrate (sample C) are shown in this study. The SVT Associates plasma source is used to supply oxygen, and standard Knudsen effusion cells were used to source Ga and Sn. Prior to the growth, the Si substrates were cleaned via multiple cycles of an internally developed process of silicon dioxide (SiO_2) formation by the UV-ozone treatment and etching in diluted HF followed by a de-ionized water rinse to remove surface contamination. Si substrates were annealed at 800 °C under vacuum ($\approx 1 \times 10^{-9}$ Torr) inside the MBE chamber for several hours to remove the native oxide layer. The last cleaning step was a Ga treatment as described elsewhere.[24] Prior to supplying oxygen to the MBE chamber, a Ga (Ga and Sn for sample B) pre-deposition for 10 min is performed at 500 °C to prevent SiO_2 formation before starting to grow the nucleation layer.[23] For Sample A, a low temperature (500 °C) nucleation layer of Ga_2O_3 was grown first (growth time 5 min, oxygen flow rate of 1.6 SCCM, and plasma power of 300 W). The substrate temperature and oxygen

flow rate were then ramped up to 660 °C and 2.5 SCCM, respectively, and the growth of Ga_2O_3 continued at a typical chamber pressure of 1.5–2.0×10^{-5} Torr. The sample was then annealed at high temperature for 2 min and cooled down slowly to avoid cracking of the film due to the thermal expansion coefficient mismatch between Ga_2O_3 and Si. For sample B, following Ga and Sn pre-deposition with a beam equivalent pressure ratio (BEP$_{Ga}$/BEP$_{Sn}$) of 25.6, low-temperature growth was carried out at an oxygen flow rate of 2.5 SCCM and plasma power of 300 W. The substrate temperature was then increased to 600 °C to increase the growth rate. Sample C was grown in two stages: in the first stage, a Ga_2O_3 layer was grown on the Si substrate following the same recipe as for sample A; TGO was then grown on the top of Ga_2O_3 using the same recipe as for sample B but with a beam equivalent pressure ratio (BEP$_{Ga}$/BEP$_{Sn}$) of 32.

The sample thicknesses were measured by cross-section scanning electron microscope (SEM) images acquired using an FEI Quanta 250 variable pressure Schottky field emission gun SEM. The structural properties were examined by conventional ω–2θ powder scan x-ray diffraction (XRD) using a PANalytical X'Pert Cu-$K_{\alpha1}$ beam ($\lambda = 1.5405$ Å). The thin film composition was analyzed by wavelength dispersive x-ray spectroscopy (WDX) in a JEOL JXA−8530F field-emission electron probe microanalyzer (EPMA) coupled with a custom-built cathodoluminescence (CL) hyperspectral imaging system. CL images were acquired with an electron beam energy of 10 keV and beam current of 40 nA. An integrated Schwarzschild reflecting objective is used to collect the emitted light, which is dispersed with an Andor Shamrock 163 spectrograph with a focal length of 163 mm, a 300 grooves/mm grating blazed at 500 nm, a 105 μm effective entrance slit (fibre optic diameter), and a 1600-channel electron-multiplying charge-coupled device (Andor Newton). Quantitative WDX data were acquired using a reduced beam energy of 6 keV, 40 nA beam current, and a 10 μm defocused spot size. The composition was determined at five measurement points across the sample and then averaged to produce the final sample composition. A peak (background) x ray counting time of 60 s (30 s) was used for all measurements. When determining the sample compositions, the following standards were used to calculate the k-ratios; bulk Ga_2O_3 for Ga and cassiterite (SnO_2) for Sn and O.

Figure 1 shows Schottky devices that were fabricated using standard photolithography methods. A Ti/Au (20 nm/100 nm) Ohmic back contact was formed on the entire rear side of the n-type Si substrate and annealed at 400 °C for 300 s in nitrogen. Formation of the front side contact consisted of two steps accomplished with a standard photolithography and lift-off procedure: (i) deposition of a high work function Pt ($\Phi_m \approx 5.5$ eV) semi-transparent layer (≈ 3 nm) and (ii) subsequent deposition of a thicker Ni/Au (20 nm/130 nm) ring contact to aid in physical probing of the device. The thin, semi-transparent Pt contact enables deep-UV light transmission (estimated at $\approx 55\%$ at $\lambda = 245$ nm) through the thin-film while still providing a suitable Schottky barrier. The current–voltage (I–V) and temporal characteristics of the Schottky photodetectors were measured with a Keithley 2450 source-meter unit using probe tips to contact specific devices on the sample surface. Spectral responsivity was measured using a Newport MS257 UV–VIS monochromator fitted with a 30 W deuterium lamp. A 305 nm high-pass filter is utilized to
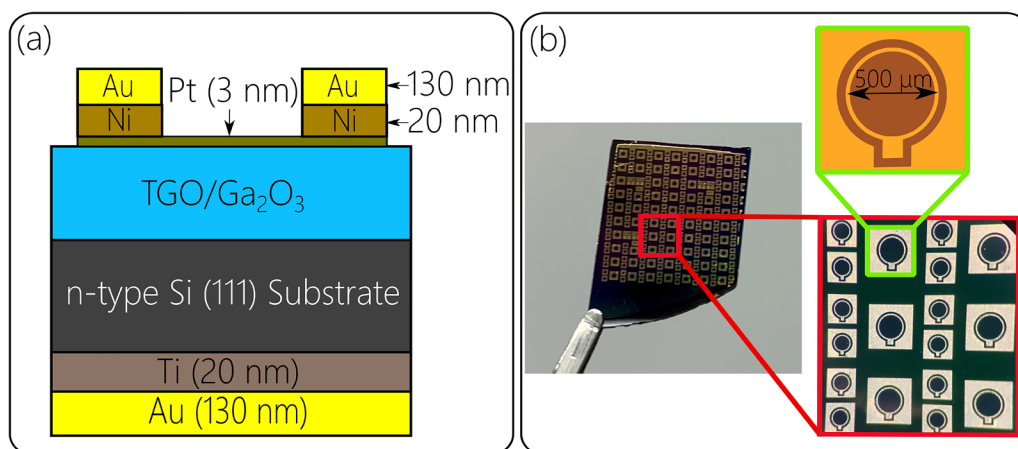
FIG. 1. (a) Schematic of a β-(Sn$_x$Ga$_{1−x}$)$_2$O$_3$ vertical Schottky barrier UV photodetector fabricated on *n*-type (111) silicon. (b) Photograph of the fabricated devices and optical microscope images showing device(s) at different scales.

remove the second-order diffraction for wavelengths longer than 310 nm. Light incident on the devices was measured using a calibrated Si photodiode to determine absolute responsivity values.

III. RESULTS AND DISCUSSION

The plan-view secondary electron images displayed in Fig. 2 reveal the surface morphology of all three samples. Distinct differences in morphology are seen for the thin film without Sn (sample A) and with Sn (samples B and C), as well as for TGO thin films without the Ga$_2$O$_3$ buffer layer (sample B) and with the Ga$_2$O$_3$ buffer layer (sample C). Nano-voids are seen for sample B, whereas sample C resulted in a smoother surface due to the underlying Ga$_2$O$_3$ buffer layer. Some nano-voids propagate to the Si substrate,

verified using the cross-section secondary electron images (see Fig. S1 in the supplementary material). The cross-section secondary electron images show the thicknesses to be 285, 1250, and 1410 nm for samples A, B, and C, respectively.

All three samples show a polycrystalline nature due to the large lattice and thermal mismatch between the thin film and the Si substrate. In order to verify the different orientations present in the grown films, XRD is performed. Figure 3 shows the dominant XRD peaks of β-Ga$_2$O$_3$ from sample A and those associated with the β-TGO from samples B and C. The buffer layer assisted growth used for sample C may reduce lattice mismatch and enhance the crystallinity of the grown film. As per the available XRD database, the preferential orientation of TGO is found to be (200), which has a peak position close to the (−201) in β-Ga$_2$O$_3$ as reported in the
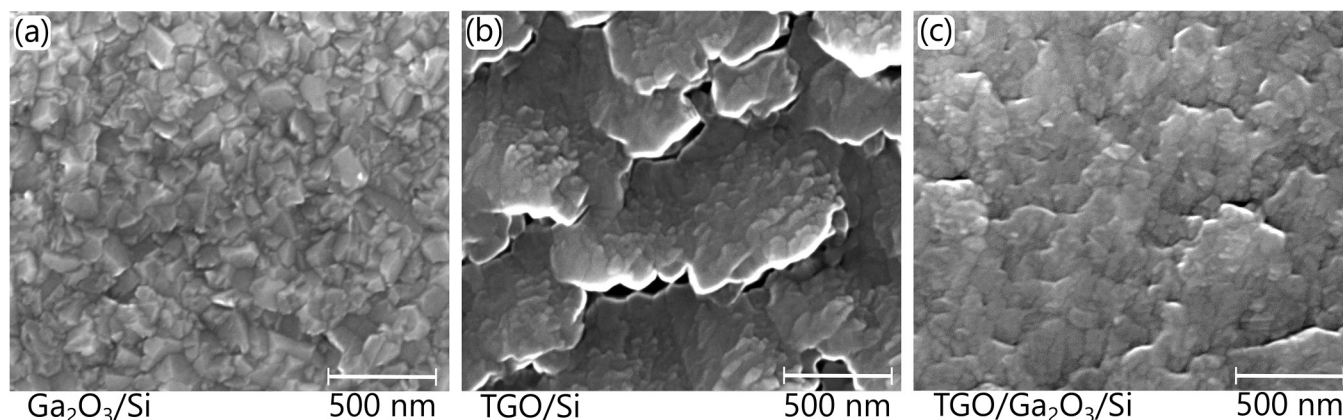

FIG. 2. Secondary electron images showing the surface morphology for (a) Ga$_2$O$_3$ thin film—sample A, (b) TGO thin film—sample B, and (c) TGO thin film with a Ga$_2$O$_3$ buffer layer—sample C. The buffer layer in sample C helps us to produce a smoother morphology without any nano-voids.
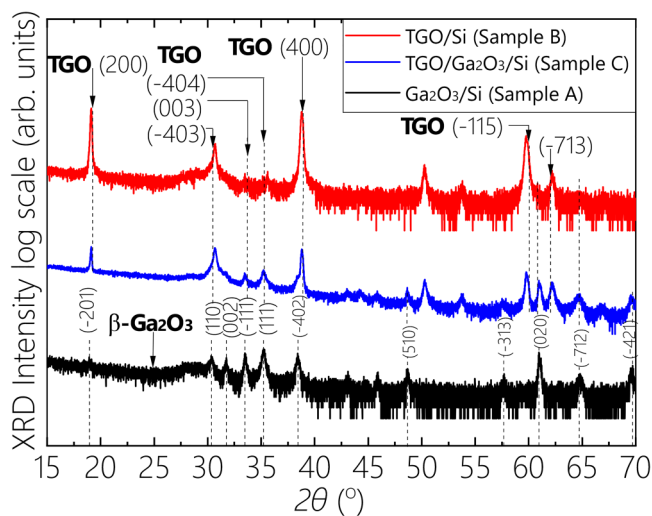
FIG. 3. XRD of polycrystalline β- Ga$_2$O$_3$ and β-(Sn$_x$Ga$_{1-x}$)$_2$O$_3$ on Si (111) substrates.

FIG. 4. Room temperature plan view CL spectroscopy for all three samples. Sample C shows the Fabry–Pérot modes from the planar cavity formed by the TGO and Ga$_2$O$_3$ buffer layer.

literature.[25–27] It is interesting to note that TGO on the Si sample has no (020) peak at 60.95°, while this is visible for the TGO/Ga$_2$O$_3$/Si and Ga$_2$O$_3$/Si samples. Furthermore, due to the thickness of the films, the Si(111) substrate peak is barely visible around 30° 2θ. The buffer layer plays an important role in obtaining a relatively smoother surface. Optimizing the buffer layer may be a way forward to produce larger crystals of preferred orientations such as (200).

The WDX microanalysis used to estimate the elemental composition shows the Sn atomic fraction percentage in samples B and C to be 0.9 and 0.8 at. %, respectively, with fractional measurement uncertainties of 0.01. The atomic percentages estimated for Ga and O are close to 40 and 60 at. %. The Sn concentration for the formula (Sn$_x$Ga$_{1-x}$)$_2$O$_3$ is calculated using the equation $x =$ [Sn (at. %)/Ga + Sn(at. %)]. Using this method, the Sn concentrations in samples B and C are calculated to be 0.022 and 0.021, respectively. The total weight percentages measured by the WDX are close to 100, indicating the validity of the measurement. However, for sample B, the weight percentage drops to around 97%, with the difference attributed to the surface morphology of this sample which has nano-voids.

Figure 4 shows room temperature CL spectra. The Ga$_2$O$_3$ thin film (sample A) shows broad emission peaks in the UV (370 nm), blue (485 nm), and red (730 nm) regions. The broad UV emission is intrinsic and is widely attributed to the recombination of free electrons and self-trapped holes (STH)[28,29] or the recombination of free electrons with self-trapped excitons (STE). The blue emission is attributed to donor–acceptor pair (DAP) recombination. The donors are created by oxygen vacancies (V$_O$), and the acceptors are created by gallium vacancies (V$_{Ga}$) or gallium–oxygen vacancy pairs (V$_{Ga}$–V$_O$).[30] The recombination mechanism responsible for the green emission (between 520 and 550 nm) is still not well understood. Previously, strong green emission was reported only
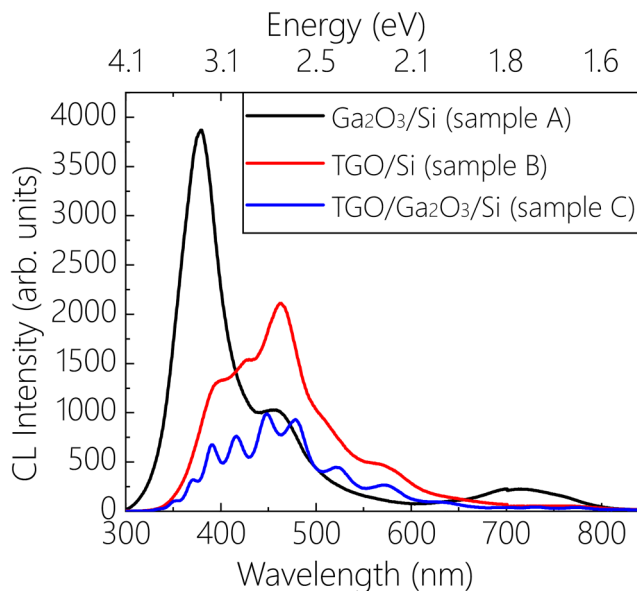
from Ga$_2$O$_3$ doped with certain elements such as Be, Mg, and Sn.[31] Oxygen interstitials have also been proposed to be the cause for green emission,[32] as has recombination between donor levels, introduced by the incorporation of Sn atoms, and holes at the valence band in Ga$_2$O$_3$.[31,33,34] The origin of the red emission is quite ambiguous, and the literature provides four plausible explanations involving doping by transition metals,[34–37] rare earth metals,[38] nitrogen, or hydrogen.[32,39] The peak structure is clarified by CL data from a cross section, as discussed in Sec. III. When compared to the CL from Sample A, the spectra for TGO samples (B and C) show a shift of the UV peak to lower energy (≈3.1 eV), which may be associated with bandgap reduction due to Sn alloying or to changes in the vacancy concentration or strain. Also, stronger green emission is observed from the TGO thin films compared with the Ga$_2$O$_3$ thin film. The multiple peaks seen in sample C are due to the Fabry–Pérot modes that arise from the difference in the refractive index of the TGO/buffer layer and the Si substrate. This effect is seen more clearly in sample C due to its smoother surface morphology [see Fig. 2(c)] when compared to sample B. The mode spacing is found to be consistent with the TGO/buffer layer thickness estimated from the cross-section SEM images (see Fig. 1 in the supplementary material).

To mitigate the effects of interference fringes seen in sample C and to understand the light emission both from the buffer layer and the TGO thin film, we have performed cross-section CL hyperspectral imaging as shown in Figs. 5 and 6. The integrated intensity image, over the measured wavelength range of 189–701 nm, [shown in Fig. 5(a)] clearly shows the high-intensity light emission from the buffer layer and the relatively low intensity from the TGO
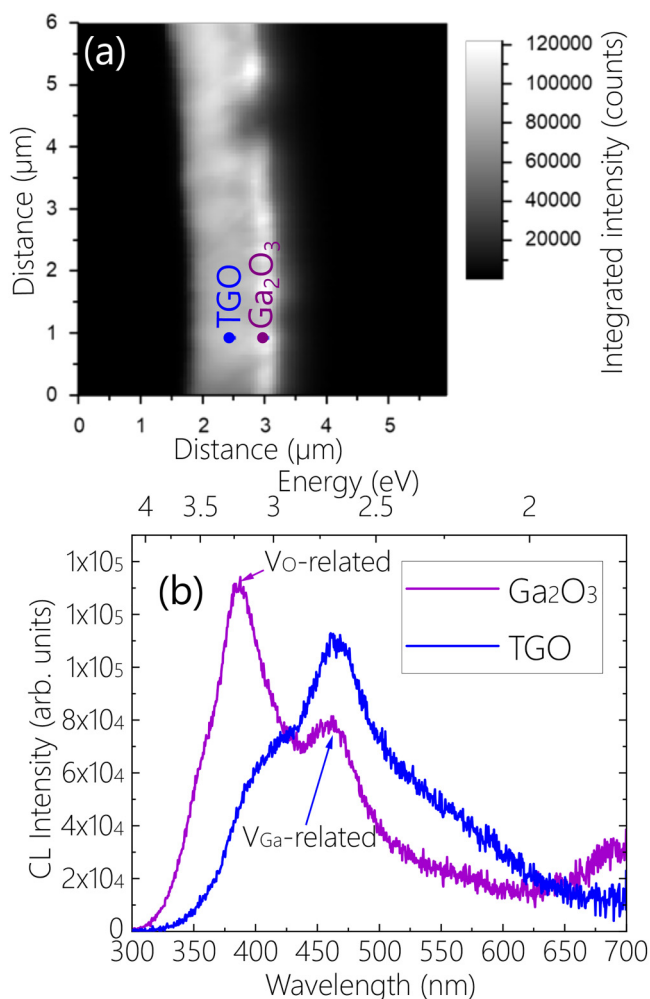
FIG. 5. Cross-section CL hyperspectral image of sample C. (a) Mean intensity map; the blue dot and purple dot are representative points in the TGO and Ga$_2$O$_3$ buffer layer and their corresponding spectra (b).

emission as well as first-order red emission. As mentioned above, H could be responsible for the red emission[39] and the addition of Sn may well form Sn–Ga or Sn–H complexes, which assist in suppressing the red emission. The origin of the reduction in the red emission when Sn is alloyed with Ga$_2$O$_3$ is still under investigation. On the other hand, the change in intensities of the UV and blue emission peaks observed in Figs 6(a) and 6(b) can be related to changes in the densities of oxygen and gallium vacancies and/or their complexes.[7,30] The influence of these vacancies on the device properties is discussed in Sec. III.

Among the various factors that determine the performance of a detector, spectral responsivity and detectivity are of great importance. The current–voltage (I–V) curves presented in Figs. 7(a)–7(c) show that the photo-to-dark current ratios are 270, 13, and 680 for the samples A, B, and C, respectively, at 5 V reverse bias under ≈25 nW (235 nm)−40 nW (258 nm) optical power. The low photo-to-dark current value for sample B is due to the high dark current, attributed to the rough surface and the nano-voids that may form interfacial defects close to the metal–semiconductor interface.[40] Figure 7(d) shows the normalized spectral responsivities with half-maximum values just below 280 nm, which is an indicator of a solar-blind photodetector. While Sample A (Ga$_2$O$_3$/Si) shows the rectifying behavior expected for a Schottky junction photodetector as shown in Fig. 7(a), samples B and C respond to UV-C light under forward bias operation [see Figs. 7(b) and 7(c)]. This implies that TGO/Ga$_2$O$_3$ and TGO/Si heterointerfaces form a larger potential barrier for electrons since the conduction band offset for Ga$_2$O$_3$/Si is very small.[41] Because of this higher potential barrier the dark current in forward bias is significantly lower than the photocurrent for the TGO samples. Therefore, Sample B and C show the photoresponse under UV light in forward bias. Detailed discussion on forward bias operation is included in in the supplementary material S3.

The peak responsivities of the photodetectors are 27.4 A/W (at 235 nm), 2011.3 A/W (at 255 nm), and 263 A/W (at 258 nm) for samples A, B, and C, respectively. These ultrahigh responsivities imply that there is a gain mechanism that can be understood via the below equation

$$R(\lambda) = \frac{\eta \, \lambda \, q}{hc} \, G,$$

where R is spectral responsivity, η is external quantum efficiency, q is the electron charge, λ is the wavelength, h is Planck's constant, c is the speed of the light in a vacuum, and G is the gain coefficient. The calculated gain-external quantum efficiency products (ηG) are 151, 9740, and 1271 for the samples A, B, and C, respectively. Note the gain would be the same as ηG, assuming a unity external quantum efficiency. These high gains are not likely to be associated with impact ionization or the STH. STH can be formed at room temperature in β-Ga$_2$O$_3$, but they will be short-lived because of recombination with electrons and due to their small thermal activation energy for migration.[42] Moreover, numerical investigation of the required hole mobility for ≈0.3 eV Schottky barrier lowering was found to be in the range of 10^{-10}–10^{-12} cm^{2}V^{-1}s^{-1}, which is much less than the theoretical hole mobility of 10^{-6} cm^{2}V^{-1}s^{-1}.[20]

layer. The Ga$_2$O$_3$ buffer layer is approximately 1.5 times brighter than the TGO layer. Representative CL spectra corresponding to these layers are displayed in Fig. 5(b), corresponding to the blue and purple dots. Each CL spectrum in the hyperspectral image was peak fitted using Gaussian functions and the heights of the fitted peaks (see supporting Fig. S2 in the supplementary material) for the UV, blue, green, and red emission are plotted as images in Figs. 6(a)–6(d) respectively. This method allows the deconvolution of peaks that would not otherwise be attainable using a simple series of monochromatic image slices. There are two striking observations from the CL intensity map: (I) the blue emission dominates in TGO and the UV emission dominates in the Ga$_2$O$_3$ buffer and (II) the reduction of red emission in the TGO layer. Our previous studies on red emission in Ga$_2$O$_3$[37] used order-sorting filters to show that the broad peak is a combination of second-order UV
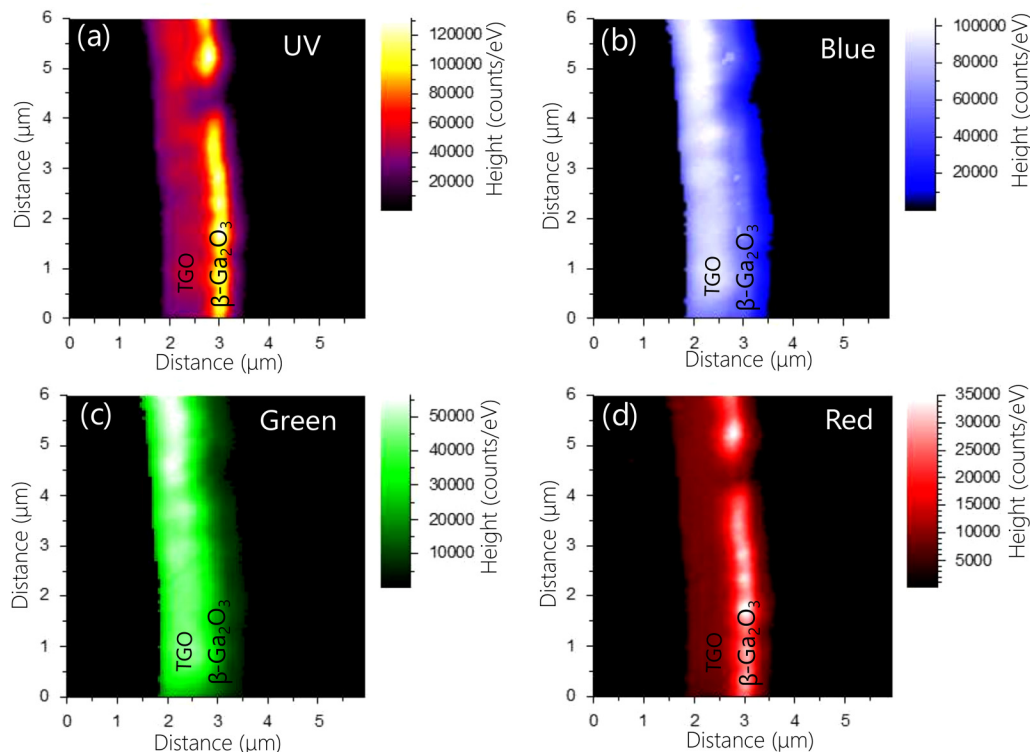
FIG. 6. Peak intensity CL maps of sample C from Gaussian fits corresponding to the (a) UV emission (3.15 eV), (b) blue emission (2.67 eV), (c) green emission (2.28 eV), and (d) red emission (1.77 eV).

Therefore, STHs are unlikely to be the reason for the observed high gains in β-Ga$_2$O$_3$ based Schottky barrier photodiodes.

Inspired from the previous studies on Schottky barrier lowering in photodetectors made of Ga$_2$O$_3$,[22,43] we propose a model (see Fig. 8) for the high gain observed in TGO photodetectors. Under UV illumination, the photogenerated electron-hole pairs are separated by the built-in voltage in the space-charge region. It is highly plausible for the accumulated holes in the space-charge region to be trapped by the deep acceptor sites, increasing the positive charge and thereby reducing the Schottky barrier and exponentially increasing the electron tunneling. The deep acceptors in our case may well be the hydrogenated gallium vacancies or the Sn–V$_{Ga}$ complexes, which may be responsible for the CL peak around 477 nm (2.6 eV). First-principle calculations reported that the optical transition from the 0 to −1 charge state for complexes with Sn is at 459.2 nm (2.7 eV),[44] close to our observed CL peak, but further literature on Sn complexes is scarce. On the other hand, previous theoretical studies on luminescence spectra in β-Ga$_2$O$_3$ assign the peak at 477 nm (2.6 eV) to hydrogenated gallium vacancies.[45] Furthermore, the reduction of red CL emission peak further supports this claim that hydrogen tends to form complexes with gallium vacancies at temperatures around 800 °C.[46] Thus, we attribute the ultrahigh gain observed in our devices to hole trapping at two possible complexes, namely, hydrogenated gallium vacancies or

Sn–V$_{Ga}$ complexes. Recently, Yakimov et al.[43] have shown a photodetector with increased photocurrent via Schottky barrier lowering by introducing deep acceptors by neutron and proton irradiation and argon plasma treatments. We adopt an alternative approach by alloying Ga$_2$O$_3$ with Sn and thereby introducing deep level acceptors and increasing the deep level trap states, which can serve as hole trapping centers as illustrated in Fig. 8. The accumulated holes in the space-charge region (SCR) increase the built-in electric field, therefore, resulting in a higher surface electric field (E$_{max}$) at the metal–semiconductor interface. Higher E$_{max}$ reduces the Schottky barrier height via the image-force lowering, also known as the Schottky effect $\left(\Delta \varphi_b = \sqrt{(qE_{max}/4\pi\varepsilon_s)} \right)$.[47] Moreover, increased positive charge in the SCR thins the width of the Schottky barrier as shown in Fig. 8. This type of thinning increases the probability of electron tunneling via thermionic-field emission and/or field emission.[47] Defining the contribution of each of these components requires a separate study, and it is out of the scope of this work. However, the contribution of each component for a Ga$_2$O$_3$ Schottky diode has been studied for power diode purposes, and the results showed that the leakage current characteristics are governed by near-ideal Schottky barrier tunneling at surface electric fields above 0.8 MV/cm.[48] Therefore, sufficient hole-trapping at the deep acceptors, introduced by Sn alloying, may be the actual reason for the extremely high gains observed in TGO Schottky barrier
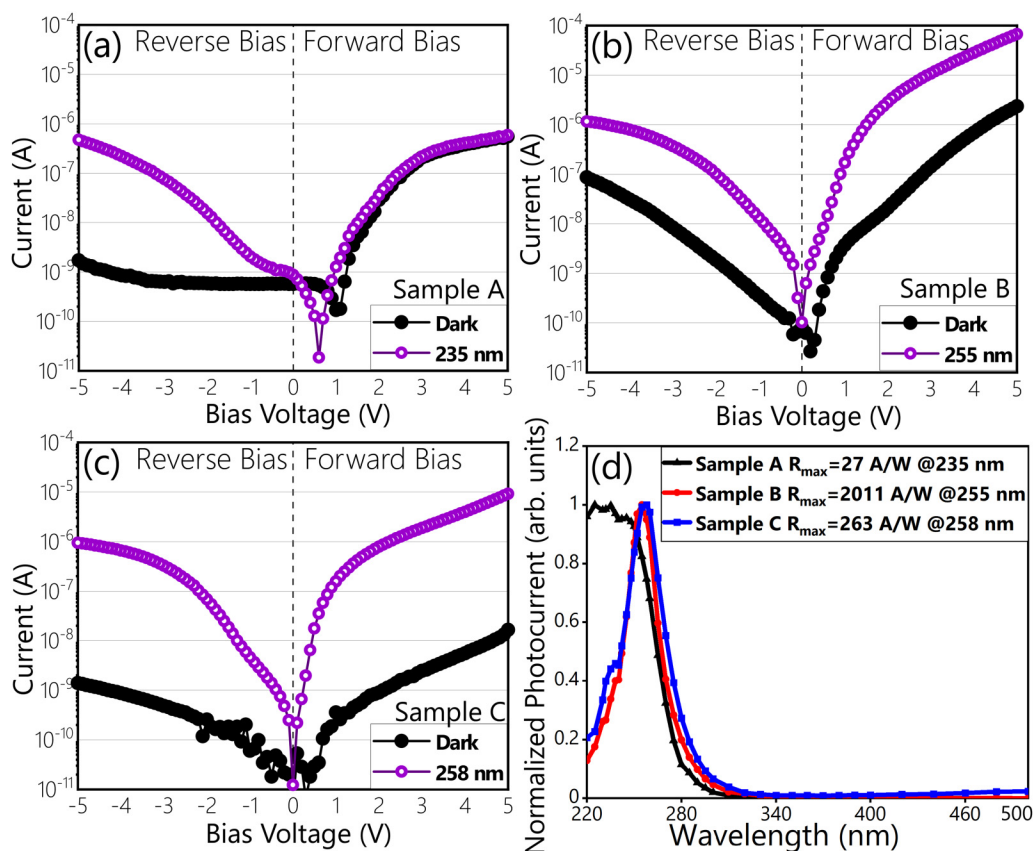
FIG. 7. Forward and reverse bias I–V curves: (a) sample A, (b) sample B, (c) sample C, and (d) normalized spectral responsivity.

photodetectors. In addition, Sn alloying can also be used to increase the UV–C coverage and improve the bandwidth of the resulting photodetector.[15–17]

While detector responsivity provides insight about the conversion efficiency of optical input to electrical output and the gain, it does not provide information about the noise characteristics, which depend on the active device area. Therefore, a critical figure of merit for a photodetector is specific detectivity ($D^\star$) expressed in Jones units $\left(\text{cm}\sqrt{\text{Hz}}/\text{W}\right)$. $D^\star$ can be used to compare two different photodetectors with different bandwidths and active areas. For deep UV photodetectors, $D^\star$ can be estimated by using the equation[49,50]

$$D^\star = R_{max}/(2eJ_{dark})^{1/2},$$

where R_{max} is the peak responsivity, e is the electron charge, and J_{dark} is the dark current density. The calculated detectivities for samples A, B, and C are 62×10^{10}, 111.3×10^{10}, and 130.6×10^{10} Jones, respectively. The increased dark current in sample B reduces the signal-to-noise ratio. Therefore, even though the responsivity is very high for sample B, the large leakage current at 5 V reverse bias results in the highest specific detectivity being for sample C as shown in Table I. The Ga_2O_3 nucleation layer has been effective in

suppressing the dark current. Figure 9 shows the transient response of the photodetectors. The transient characteristics of a photodetector directly define its limit in applications requiring a fast response. The rise and fall times are calculated by fitting the transient data with a double exponential function as shown in the below equation

$$I(t) = I_0 + Ae^{-t/\tau 1} + Be^{-t/\tau 2}.$$

Alloying Ga_2O_3 with Sn does not seem to significantly affect the rise times as seen in Table I. However, fall times are noticeably decreased in the TGO devices, with values of 0.5–0.8 s compared to 1.2 s for the Ga_2O_3 device. It has been shown that the slow decay time (τ_{f2}) is proportional to the density of oxygen vacancies in Ga_2O_3[51] and $(In_xGa_{1-x})_2O_3$.[8] As shown in Fig. 5(b), the oxygen vacancy related CL emission peak for TGO is significantly lower than for the Ga_2O_3 thin-film. Therefore, electron trapping/detrapping at oxygen vacancy-related traps may be the reason for the faster decay times observed for TGO devices as shown in Fig. 9. Moreover, electrons have a higher probability of trapping multiple times since they travel through the entire thin film. On the other hand, holes only travel a short distance to the Schottky contact due to the exponentially-decreasing light absorption profile. Once
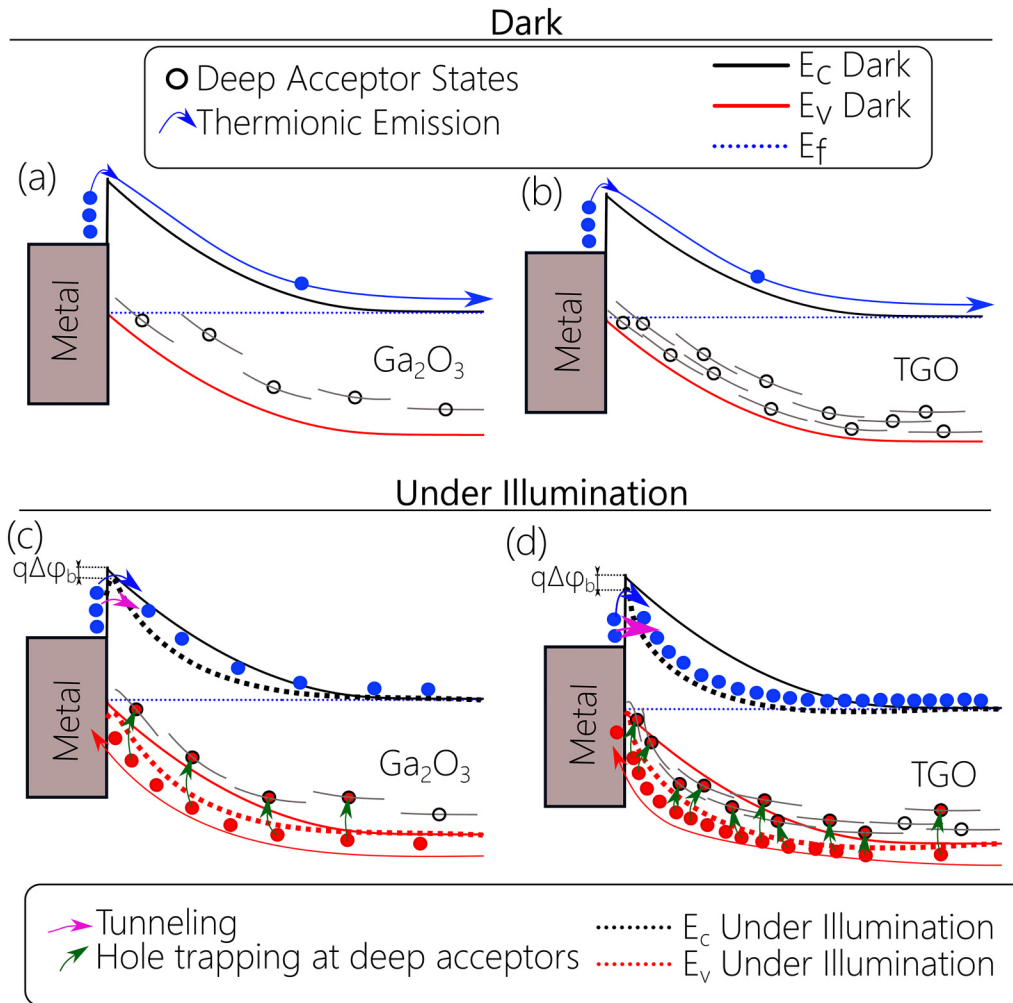
FIG. 8. Schematic representation of the gain mechanism in Ga$_2$O$_3$ and (Sn$_x$Ga$_{1-x}$)$_2$O$_3$ (TGO) based photodetectors. Carrier transport in Ga$_2$O$_3$ (a) and TGO (b) under dark conditions where the Schottky barrier is dominated by thermionic emission of majority carriers. Hole trapping-assisted gain mechanism under UV illumination in Ga$_2$O$_3$ (c) and TGO (d) photodetectors.

electrons populate the traps, the de-trapping and collection process will likely increase the decay time. The minor difference in transient between samples B and C may originate from the buffer layer, which may affect the valence and conduction band offsets with the TGO layer. We have also compared the forward and reverse bias transient responses for sample B (see Fig. S3 in the supplementary material), showing that reverse bias operation is preferred for better photodetector parameters.

TABLE I. Summary of growth conditions, alloy composition, and device characteristics.

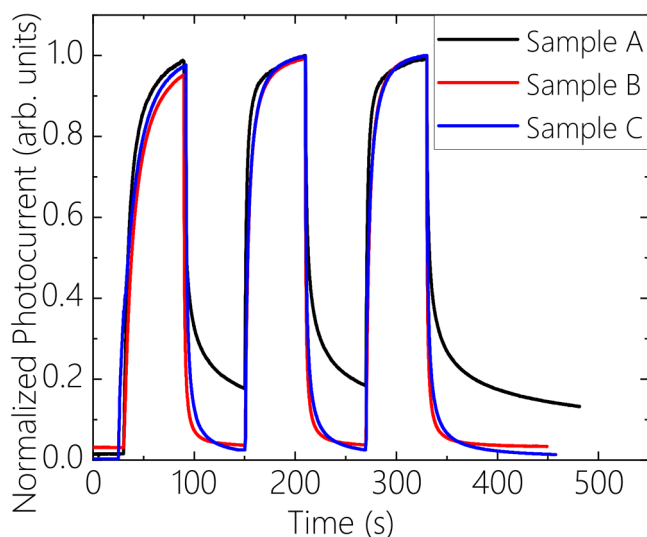| Sample	Tsub (°C)	$\frac{\text{BEP (Ga)}}{\text{BEP (Sn)}}$	Sn , x	Rise time $\tau_{\text{r (s)}}$	Fall time $\tau_{\text{f (s)}}$	Peak responsivity (A/W)	Detectivity ($\times 10^{10}$ Jones)
A	660	0	0	$\tau_{r1} = 1.7$ $\tau_{r2} = 16.8$	$\tau_{f1} = 1.2$ $\tau_{f2} = 15.0$	27.4 (@ 235 nm)	62.0
B	600	25.6	0.0220 ± 0.0006	$\tau_{r1} = 2.9$ $\tau_{r2} = 13.6$	$\tau_{f1} = 0.5$ $\tau_{f2} = 5.1$	2011 (@ 255 nm)	111.3
C	600	32	0.0210 ± 0.0005	$\tau_{r1} = 2.1$ $\tau_{r2} = 11.0$	$\tau_{f1} = 0.8$ $\tau_{f2} = 8.2$	263 (@ 258 nm)	130.6

FIG. 9. Normalized transient characteristics for Ga_2O_3 (sample A) and TGO photodetectors (samples B and C).

IV. SUMMARY AND CONCLUSION

We have demonstrated the heterogeneous integration of $(Sn_xGa_{1-x})_2O_3$ (TGO) UV–C photodetectors on silicon substrates by plasma assisted MBE and studied the functional properties of fabricated devices. Our results show that a TGO detector with a Ga_2O_3 buffer layer exhibits a better device performance when compared to one without the buffer layer. Best $TGO/Ga_2O_3/Si$ devices had peak responsivities of ≈ 260 A/W with detectivities on the order of 10^{12} Jones. Cross-section CL images show a correlation between the increase in deep-level acceptors and the increase in photocurrent. The observed high gain is attributed to the combination of Schottky barrier lowering, increased thermionic-field emission, and/or field emission due to hole trapping at deep-level traps. This work demonstrates the viability of TGO UV–C solar-blind detectors on Si substrates and is a step forward for $p-n$ heterojunction photodiodes.

SUPPLEMENTARY MATERIAL

See the supplementary material for the cross-section SEM images and the fitted CL spectra, thin film thickness estimated from the Fabry–Pérot modes, and the comparison of reverse bias and forward bias transient responses.

AUTHOR DECLARATIONS

Conflict of Interest

The authors declare no competing financial interests.

Author Contributions

I.H. and D.A.H. contributed equally to this work.

DATA AVAILABILITY

The data that support the findings of this study are openly available in University of Strathclyde research portal at http://doi.org/10.15129/d2eaa892-20e9-4e60-9f4c-7169a245a449, Ref. 52. Alternatively, they are also available from the corresponding author upon reasonable request.

REFERENCES

[1]M.-P. Zorzano, J. Martin-Soler, J. Gomez-Elvir, and J.-W. Shi, *Photodiodes—Communications, Bio-Sensings, Measurements and High-Energy Physics* (IntechOpen, 2011).
[2]D. Kedar and S. Arnon, Opt. Eng. **48**(4), 046001 (2009).
[3]P. A. Scowen, M. R. Perez, S. G. Neff, and D. J. Benford, Exp. Astron. **37**, 11 (2014).
[4]Z. Alaie, S. M. Nejad, and M. H. Yousefi, Mater. Sci. Semicond. Process. **29**, 16 (2015).
[5]F. Alema, B. Hertog, O. Ledyaev, D. Volovik, R. Miller, A. Osinsky, S. Bakhshi, and W. V. Schoenfeld, Sens. Actuators, A **249**, 263 (2016).
[6]E. Cicek, R. McClintock, C. Y. Cho, B. Rahnema, and M. Razeghi, Appl. Phys. Lett. **103**, 191108 (2013).
[7]S. J. Pearton, J. Yang, P. H. Cary, F. Ren, J. Kim, M. J. Tadjer, and M. A. Mastro, Appl. Phys. Rev. **5**, 011301 (2018).
[8]I. Hatipoglu, P. Mukhopadhyay, F. Alema, T. S. Sakthivel, S. Seal, A. Osinsky, and W. V. Schoenfeld, J. Phys. D: Appl. Phys. **53**, 454001 (2020).
[9]J. E. N. Swallow, R. G. Palgrave, P. A. E. Murgatroyd, A. Regoutz, M. Lorenz, A. Hassa, M. Grundmann, H. Von Wenckstern, J. B. Varley, and T. D. Veal, ACS Appl. Mater. Interfaces **13**, 2807 (2021).
[10]R. Miller, F. Alema, and A. Osinsky, IEEE Trans. Semicond. Manuf. **31**, 467 (2018).
[11]M. A. Mastro, J. K. Hite, C. R. Eddy, M. J. Tadjer, S. J. Pearton, F. Ren, and J. Kim, Int. J. High Speed Electron. Syst. **28**, 1940007 (2019).
[12]J. Zhou, H. Chen, H. Fu, K. Fu, X. Deng, X. Huang, T. H. Yang, J. A. Montes, C. Yang, X. Qi, B. Zhang, X. Zhang, and Y. Zhao, Appl. Phys. Lett. **115**, 251108 (2019).
[13]S. Tan, H. Deng, K. E. Urbanek, Y. Miao, Z. Zhao, J. S. Harris, and R. L. Byer, Opt. Express **28**, 12475 (2020).
[14]T. Matsuda, K. Umeda, Y. Kato, D. Nishimoto, M. Furuta, and M. Kimura, Sci. Rep. **7**, 44326 (2017).
[15]P. Mukhopadhyay and W. V. Schoenfeld, Appl. Opt. **58**, D22 (2019).
[16]P. Mukhopadhyay and W. V. Schoenfeld, J. Vac. Sci. Technol., A **38**, 013403 (2020).
[17]P. Mukhopadhyay, M. Toporkov, and W. V. Schoenfeld, "Oxide-based materials and devices IX" Proc. SPIE **10533**, 105330 (2018).
[18]T. Oshima, T. Okuno, N. Arai, N. Suzuki, S. Ohira, and S. Fujita, Appl. Phys. Express **1**, 011202 (2008).
[19]A. M. Armstrong, M. H. Crawford, A. Jayawardena, A. Ahyi, and S. Dhar, J. Appl. Phys. **119**, 103102 (2016).
[20]F. Akyol, Turk. J. Phys. **45**, 169 (2021).
[21]B. E. Kananen, N. C. Giles, L. E. Halliburton, G. K. Foundos, K. B. Chang, and K. T. Stevens, J. Appl. Phys. **122**, 215703 (2017).

[22]E. B. Yakimov, A. Y. Polyakov, I. V. Shchemerov, N. B. Smirnov, A. A. Vasilev, P. S. Vergeles, E. E. Yakimov, A. V. Chernykh, A. S. Shikoh, F. Ren, and S. J. Pearton, APL Mater. **8**, 111105 (2020).

[23]P. Mukhopadhyay, I. Hatipoglu, T. S. Sakthivel, D. A. Hunter, P. R. Edwards, R. W. Martin, G. Naresh-Kumar, S. Seal, and W. V. Schoenfeld, Adv. Photonics Res. **2**, 2000067 (2021).

[24]P. Mukhopadhyay, S. Chowdhury, A. Wowchak, A. Dabiran, P. Chow, and D. Biswas, J. Vac. Sci. Technol., B **31**, 03C132 (2013).

[25]X. Chen, K. Liu, Z. Zhang, C. Wang, B. Li, H. Zhao, D. Zhao, and D. Shen, ACS Appl. Mater. Interfaces **8**, 4185 (2016).

[26]P. Li, H. Shi, K. Chen, D. Guo, W. Cui, Y. Zhi, S. Wang, Z. Wu, Z. Chen, and W. Tang, J. Mater. Chem. C **5**, 10562 (2017).

[27]K. Arora, N. Goel, M. Kumar, and M. Kumar, ACS Photonics **5**, 2391 (2018).

[28]T. Gake, Y. Kumagai, and F. Oba, Phys. Rev. Mater. **3**, 044603 (2019).

[29]A. Kyrtsos, M. Matsubara, and E. Bellotti, Appl. Phys. Lett. **112**, 032108 (2018).

[30]L. Binet and D. Gourier, J. Phys. Chem. Solids **59**, 1241 (1998).

[31]T. Harwig and F. Kellendonk, J. Solid State Chem. **24**, 255 (1978).

[32]Q. D. Ho, T. Frauenheim, and P. Deák, Phys. Rev. B **97**, 115163 (2018).

[33]Y. P. Song, H. Z. Zhang, C. Lin, Y. W. Zhu, G. H. Li, F. H. Yang, and D. P. Yu, Phys. Rev. B **69**, 075304 (2004).

[34]I. López, E. Nogales, B. Méndez, J. Piqueras, A. Peche, J. Ramírez-Castellanos, and J. M. González-Calbet, J. Phys. Chem. C **117**, 3036 (2013).

[35]R. Sun, Y. K. Ooi, P. T. Dickens, K. G. Lynn, and M. A. Scarpulla, Appl. Phys. Lett. **117**, 052101 (2020).

[36]A. Luchechko, V. Vasyltsiv, Ya. Zhydachevskyy, M. Kushlyk, S. Ubizskii, and A. Suchocki, J. Phys. D: Appl. Phys. **53**, 354001 (2020).

[37]G. Naresh-Kumar, H. MacIntyre, S. Subashchandran, P. R. Edwards, R. W. Martin, K. Daivasigamani, K. Sasaki, and A. Kuramata, Phys. Status Solidi B **258**, 2000465 (2021).

[38]P. Marwoto, S. Sugianto, and E. Wibowo, J. Theor. Appl. Phys. **6**, 17 (2012).

[39]T. T. Huynh, E. Chikoidze, C. P. Irvine, M. Zakria, Y. Dumont, F. H. Teherani, E. V. Sandana, P. Bove, D. J. Rogers, M. R. Phillips, and C. Ton-That, Phys. Rev. Mater. **4**, 085201 (2020).

[40]R. T. Tung, Appl. Phys. Rev. **1**, 011304 (2014).

[41]M. K. Yadav, A. Mondal, S. Das, S. K. Sharma, and A. Bag, J. Alloys Compd. **819**, 153052 (2020).

[42]S. Yamaoka, Y. Furukawa, and M. Nakayama, Phys. Rev. B **95**, 094304 (2017).

[43]E. B. Yakimov, A. Y. Polyakov, I. V. Shchemerov, N. B. Smirnov, A. A. Vasilev, A. I. Kochkova, P. S. Vergeles, E. E. Yakimov, A. V. Chernykh, M. Xian, F. Ren, and S. J. Pearton, J. Alloys Compd. **879**, 160394 (2021).

[44]A. Singh, O. Koksal, N. Tanen, J. McCandless, D. Jena, H. G. Xing, H. Peelaers, and F. Rana, Phys. Rev. Res. **3**, 023154 (2021).

[45]Y. K. Frodason, K. M. Johansen, L. Vines, and J. B. Varley, J. Appl. Phys. **127**, 075701 (2020).

[46]A. Y. Polyakov, I. H. Lee, N. B. Smirnov, E. B. Yakimov, I. V. Shchemerov, A. V. Chernykh, A. I. Kochkova, A. A. Vasilev, F. Ren, P. H. Carey, and S. J. Pearton, Appl. Phys. Lett. **115**, 032101 (2019).

[47]S. M. Sze and K. K. Ng, *Physics of Semiconductor Devices*, 3rd ed. (John Wiley Sons, Inc., Hoboken, NJ, 2007).146.

[48]W. Li, D. Saraswat, Y. Long, K. Nomoto, D. Jena, and H. G. Xing, Appl. Phys. Lett. **116**, 192101 (2020).

[49]A. S. Pratiyush, S. Krishnamoorthy, R. Muralidharan, S. Rajan, and D. N. Nath, Gallium Oxide Technol. Devices Appl. **16**, 369 (2018).

[50]Y. Fang, A. Armin, P. Meredith, and J. Huang, Nat. Photonics **13**, 1 (2019).

[51]D. Y. Guo, Z. P. Wu, Y. H. An, X. C. Guo, X. L. Chu, C. L. Sun, L. H. Li, P. G. Li, and W. H. Tang, Appl. Phys. Lett. **105**, 023507 (2014).

[52]I. Hatipoglu, D. A. Hunter, P. Mukhopadhyay, M. S. Williams, P. R. Edwards, R. W. Martin, W. V. Schoenfeld, and G. Naresh-Kumar, "Data for: Correlation between deep-level defects and functional properties of β-(Sn$_x$Ga1$_{-x}$)2O3 on Si photodetectors," (to be published 2021); available at https://pureportal.strath.ac.uk/en/publications/correlation-between-deep-level-defects-and-functional-properties-